



Radio Science®

RESEARCH ARTICLE

10.1029/2021RS007372

Key Points:

- Using interferometry, magnetic field fluctuations can be measured with bright, unpolarized cosmic radio sources
- Examples presented here show fluctuations with amplitudes
 ~10-30 nT and oscillation periods
 ~10-40 min on a scale of 75 km
- These perturbations could plausibly be tied to changes in the background electric field driven by gravity waves with amplitudes ~10 m s⁻¹

Correspondence to:

J. F. Helmboldt, joseph.helmboldt@nrl.navy.mil

Citation

Helmboldt, J. F., Clarke, T. E., & Kassim, N. E. (2022). Remote sensing of mid-latitude ionospheric magnetic field fluctuations using cosmic radio sources. *Radio Science*, *57*, e2021RS007372. https://doi.org/10.1029/2021RS007372

Received 24 SEP 2021 Accepted 8 APR 2022

Author Contributions:

Clarke, N. E. Kassim

Data curation: J. F. Helmboldt

Formal analysis: J. F. Helmboldt

Funding acquisition: T. E. Clarke

Investigation: J. F. Helmboldt

Methodology: J. F. Helmboldt, T. E.

Clarke, N. E. Kassim

Project Administration: T. E. Clarke

Resources: T. E. Clarke

Software: J. F. Helmboldt

Supervision: N. E. Kassim

Visualization: J. F. Helmboldt

Writing – original draft: J. F. Helmboldt

Writing – review & editing: J. F.

Helmboldt, T. E. Clarke, N. E. Kassim

Concentualization: L.F. Helmboldt, T.E.

Published 2022. This article is a U.S. Government work and is in the public domain in the USA.

Remote Sensing of Mid-Latitude Ionospheric Magnetic Field Fluctuations Using Cosmic Radio Sources

J. F. Helmboldt¹, T. E. Clarke¹, and N. E. Kassim¹

¹US Naval Research Laboratory, Washington, DC, USA

Abstract This paper describes a new method for remote sensing of magnetic field fluctuations at ionospheric altitudes using a relatively long-baseline interferometer and exceptionally bright cosmic radio sources at 35 MHz. The technique uses sensitive measurements of the difference in phase between two phased array telescopes separated by about 75 km and between the right and left circular polarizations to measure the amount of differential Faraday rotation. Combined with estimates of the background magnetic field and total electron content, these can be converted to measurements of fluctuations in the differential magnetic field parallel to the line of sight, ΔB_{\parallel} . The temporal gradient in ΔB_{\parallel} roughly follows the diurnal pattern expected for B_{\parallel} due to the vertical gradient in the background electric field, but at roughly 25% the magnitude and offset by ~50 nT hr⁻¹. This suggests that the diurnal variation in the electric fields observed by the two telescopes are similar but slightly different ($|\Delta E| \lesssim 0.1$ mV m⁻¹). Fluctuations in ΔB_{\parallel} were typically ~10–30 nT with wavelike fluctuations often apparent. These typically have oscillation periods of about 10–30 min, similar to traveling ionospheric disturbances (TIDs). Simultaneous observations toward two sources separated by 25.4° on the sky (~140 km in the F-region) show a few detections of wavelike disturbances with lags of ± 10 –30 min between them. These imply speeds on the order of 100–200 m s⁻¹, also similar to TIDs. We estimate that gravity waves with amplitudes within the dynamo region of ~10 m s⁻¹ could generate the observed fluctuations in ΔB_{\parallel} .

1. Introduction

The Earth's magnetic field is quite stable at its surface and throughout the atmosphere. Small-amplitude fluctuations (<1%) are relatively common at the surface at high latitudes in the auroral zone where the magnetic field lines map to the magnetosphere and are heavily influenced by the solar wind. These fluctuations increase significantly during geomagnetically active times, but still amount to only a few percent of the background field strength. At mid-latitudes, where the magnetic field lines are well insulated from the impact of the solar wind, these fluctuations are even smaller. However, even within the mid-latitude ionosphere, which is nearly always geomagnetically quiet, there are several well-known current systems. These include solar quiet (Sq) currents (Yamazaki & Maute, 2017), dynamo currents (Lühr & Maus, 2006), currents driven by irregularities (Park et al., 2009), and gravity-driven currents (Maus & Lühr, 2006).

Current systems throughout the ionosphere have been well studied in situ using magnetometers onboard low Earth orbiting (LEO) satellites such as the Challenging Minisatellite Payload (CAMP) mission. However, the nature of these measurements are not conducive to characterizing spatial gradients within such current systems unless they are present along the flight path of the satellite. Disturbances within the drivers of these current systems can therefore lead to spatial variations that may be overlooked by such measurements. In particular, perturbations within the neutral wind, especially within the dynamo region (~100–140 km altitude) where the ion/neutral collision rate exceeds the ions' gyrofrequencies, will alter the electric field and likewise the magnetic field.

Atmospheric gravity waves are relatively common neutral wind disturbances that often propagate to the upper atmosphere (e.g., Becker and Vadas, 2018; Tsuda, 2014; Vadas and Fritts, 2002). Within the thermosphere, their impact on the ion/electron density manifests as traveling ionospheric disturbances (TIDs) with wavelengths on the order of 100 km (e.g., Hickey et al., 2009; Hooke, 1968; Vadas and Crowley, 2010). Due to the high conductivity along magnetic field lines within the ionosphere, alterations in the dynamo-driven electric field due to gravity waves can have impacts beyond the thermosphere into the plasmasphere (Helmboldt et al., 2020) and to the conjugate hemisphere (Huba et al., 2015). Nighttime TIDs have been shown to produce their own polarization

HELMBOLDT ET AL. 1 of 13

electric fields via the Perkins instability (Perkins, 1973) which have been observed with airglow imagers to map to the conjugate point (Otsuka et al., 2004).

The spatially and temporally oscillating nature of these electric field perturbations implies that they must also have an impact on the local magnetic field. While these may be relatively small in magnitude, their impact on systems that require a very stable and/or accurately specified magnetic field could be significant. For instance, the next generation of interferometric radio telescopes operating in the meter-wave and microwave regimes are aiming for larger separations among individual antennas/elements to achieve high resolutions required to meet their science goals. These include the Next Generation Very Large Array (ngVLA; Murphy et al., 2018) and the Square Kilometer Array (SKA; Quinn et al., 2015). The ability to perform accurate polarimetric imaging of linearly polarized cosmic radio sources could be compromised by significant differences in the ionospheric magnetic field along the lines of sight of the antennas within these arrays due to the Faraday effect.

It is this differential Faraday effect that makes interferometric telescopes uniquely sensitive instruments for measuring spatial gradients within the ionospheric magnetic field, especially at mid-latitudes where these gradients are likely quite subtle. Within this paper, we describe a novel method for using the Faraday effect to detect and quantify differences in the line of sight magnetic field between two radio telescopes observing the same cosmic radio source. These telescopes comprise the Long Wavelength Array (LWA) interferometer in New Mexico, which operates in the 20–80 MHz frequency range. By observing bright sources with the LWA telescopes at a low VHF frequency (35 MHz) and with a relatively long baseline (75 km), the difference in the ionospheric delay between the two circular polarizations is measurable. Thus, even without a polarized source, the Faraday effect can be used with this experimental setup to establish an ionospheric magnetic gradiometer. In Section 2, we detail the data and analysis with conclusions given in Section 3.

2. Data and Analysis

2.1. Observations and Processing

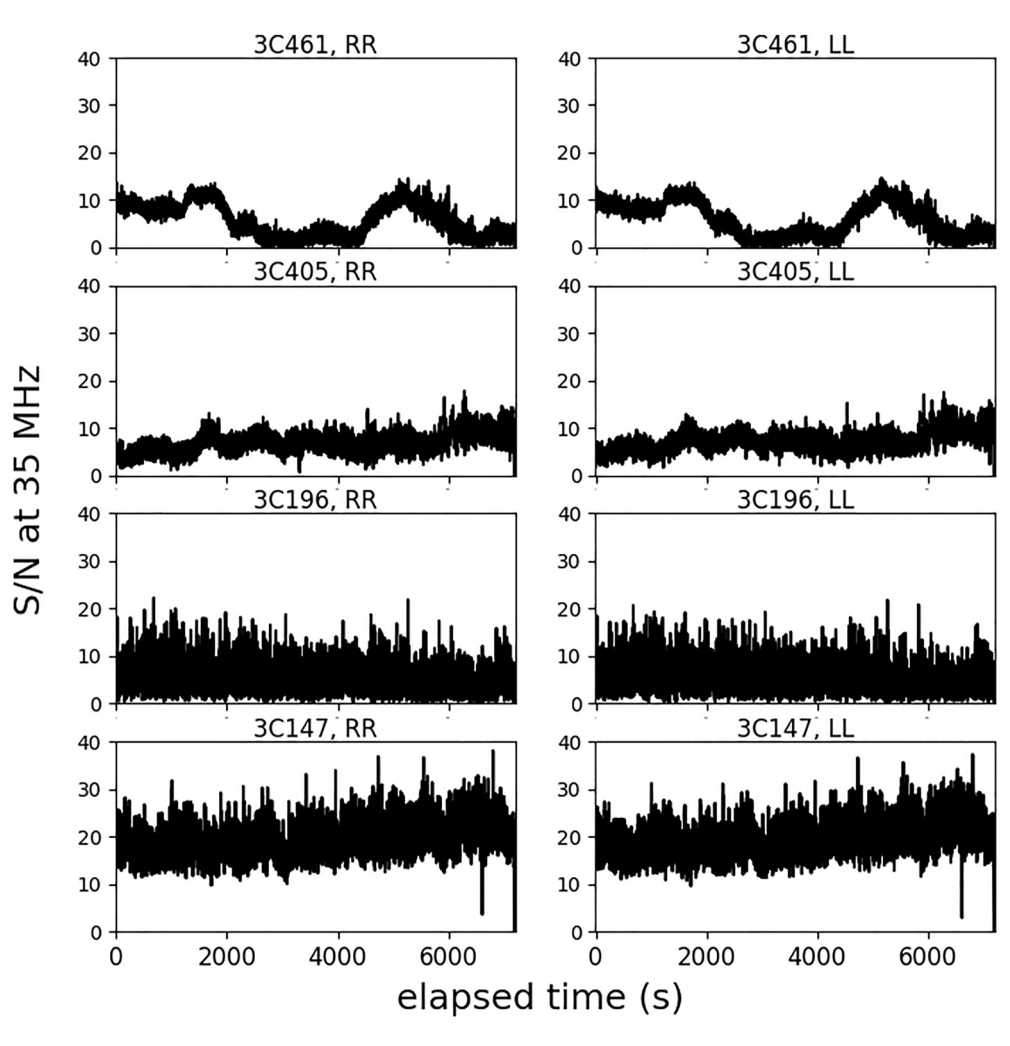
As mentioned in Section 1, measurements of differential Faraday rotation were undertaken with the LWA interferometer (Davis et al., 2020). There are currently two LWA "stations," a term used to denote a single phased array of 256 inverted vee dipole antennas that are quasi-randomly distributed within a roughly 100-m diameter area (Taylor et al., 2012). One station, LWA1, is near the site of the VLA telescope on the Plains of San Agustin in New Mexico. The other is located approximately 75 km away, east by northeast, near the Sevilleta National Wildlife Refuge, and is referred to as LWA-SV. Several two-hour observing sessions were conducted during 2019 with each station electronically forming two beams, one on each of a pair of extremely bright cosmic radio sources that are in the same region of the sky. Each session was scheduled to be centered on the mean transit time of the two sources to maximize their elevations and minimize polarization leakage (Clarke et al., 2014).

Two frequency bands were used centered at 35 and 45 MHz, each 9.8 MHz wide. Complex voltages recorded with both linear polarizations at both stations were cross-correlated to produce right and left hand circular polarization visibilities per beam and frequency band. These were "fringe stopped" toward each source, that is, the expected delay between the two stations for each source was accounted for during the correlation process. The visibilities were generated with a 1-s integration time and 256 frequency channels per band to facilitate the flagging of spurious data. Times/frequencies where the visibility amplitude was larger than the median by more than seven times the median absolute deviation (MAD) were flagged prior to averaging over all frequencies within a single band.

Two sets of well-known cosmic radio sources were used: 3C405 with 3C461 and 3C147 with 3C196. These pairs are separated by 36.4° and 25.4° on the sky, respectively. While the integrated flux densities of 3C405 and 3C461 are many times larger than those of 3C147 and 3C196, they are also well resolved by the LWA interferometer, and thus can appear fainter within the resulting visibility amplitudes. This is shown in Figure 1, which shows the signal-to-noise ratio, S/N, at 35 MHz for each source in right (RR) and left (LL) circular polarization as functions of elapsed time from example observing sessions. One can see that at the resolution of the LWA interferometer, 3C147 is actually the brightest source and that 3C461 is only marginally detected at times due to its relatively large angular size and ring-like structure (de Gasperin et al., 2020) and the orientation/length of the interferometer.

For each source, the RR visibility phase is given by

HELMBOLDT ET AL. 2 of 13



onlinelibrary.wiley.com/doi/10.1029/2021RS007372 by University Of New Mexico, Wiley Online Library on [25/10/2023]. See the Terms and Conditions (https://www.co.wiley.com/doi/10.1029/2021RS007372 by University Of New Mexico, Wiley Online Library on [25/10/2023]. See the Terms and Conditions (https://www.co.wiley.com/doi/10.1029/2021RS007372 by University Of New Mexico, Wiley Online Library on [25/10/2023]. See the Terms and Conditions (https://www.co.wiley.com/doi/10.1029/2023).

Figure 1. From example observing sessions, the S/N at 35 MHz versus elapsed time for each of the four observed sources using (left panels) the right circular polarization (RR) and (right panels) the left circular polarization (LL). In all cases, the noise was computed using the cross correlations between opposite polarizations (i.e., RL and LR) which are dominated by noise due to the unpolarized nature of the sources. We note that this ignores the impact of confusion, which is virtually non-existent within the RL and LR data due to nearly all emission from the sky at 35 MHz being unpolarized.

$$\phi_{RR} = \phi_{source} + \phi_{inst} + \phi_{noise} + n2\pi + 8436 \left(\frac{\Delta TEC}{1 \text{ TECU}}\right) \left(\frac{\nu}{1 \text{ MHz}}\right)^{-1}$$
(1)

where ϕ_{source} is the contribution due to source structure; ϕ_{inst} is the instrumental contribution, which is typically quite stable and essentially constant over a session; ϕ_{noise} is the contribution from noise; n is an integer; and ν is the observing frequency. The difference in the total electron content (TEC) between the two stations' lines of sight is given by Δ TEC in the typical units of TECU (1 TECU = 10^{16} m⁻²). With sufficiently high S/N (>5), the 2π ambiguity contribution can be effectively eliminated by unwrapping the phase time series except for the initial value of $n2\pi$ at the beginning of the time series. That initial value can effectively be folded into the ϕ_{inst} term. The source contribution is only approximately known based on models of the source, but will repeat with local sidereal time (LST). Since the observing sessions were all timed to center on the mean transit time of each pair of sources, they span the same range in LST (per source). This means that trends with LST can be used to determine any residual effects due to ϕ_{source} (more on this later).

The Faraday effect will cause the RR and LL phase to differ by an amount given by

$$\phi_{RR} - \phi_{LL} = 4.71 \times 10^8 \left(\frac{\Delta RM}{1 \text{ TECUT}}\right) \left(\frac{v}{1 \text{ MHz}}\right)^{-2} \tag{2}$$

HELMBOLDT ET AL. 3 of 13

$$RM = \int B_{\parallel} N_e dS \approx B_{\parallel}(z = \text{hmF2}) TEC$$
 (3)

where B_{\parallel} is the component of Earth's magnetic field that is parallel to the line of sight, S, and RM is the rotation measure. Here, we have expressed RM in units of TECU T, but these can be converted to the units more commonly used within astronomy, radians m⁻², by multiplying by 2620. If the ionosphere is treated as a thin shell, the approximation on the right hand side of Equation 3 holds, where B_{\parallel} is calculated at the peak height denoted by the ionosonde parameter hmF2 according to the International Geomagnetic Reference Field (IGRF).

Within each two-hour observation window, we assume that the line-of-sight TEC and magnetic fields can be approximated as TEC = $\csc(e)$ [$T + d_T(t, x)$] and $B_{\parallel} = b_{\parallel}(e, a)$ [$B + d_B(t, x)$]. Here, e and a are elevation and azimuth, respectively, b_{\parallel} is the component of the magnetic field unit vector parallel to the line of sight, T and B are constants, and d_T and d_B are small perturbation terms such that $d_T d_B \simeq 0$. Using this formulation with Equations 1 and 2, the difference in RM between the two telescopes is

$$\Delta RM = \csc(e)b_{\parallel}(e, a) \left\{ T \left[d_B(t, x_1) - d_B(t, x_2) \right] + B \left[d_T(t, x_1) - d_T(t, x_2) \right] \right\}$$
(4)

and $\Delta B_{\parallel} = b_{\parallel} \Delta d_{B}$. The quantity $\csc(e) \Delta d_{T}$ can be computed (with some instrumental/source bias) from the unwrapped ϕ_{RR} measurements. Both B and b_{\parallel} can be computed from the IGRF. The low-resolution, GPS-based TEC maps generated by the Jet Propulsion Laboratory (JPL) provide a means to compute $\csc(e)T$, or "slant" TEC (STEC). For this, we used the JPL IONEX files and functions within the RMextract python package (https://github.com/lofar-astron/RMextract). We note that these TEC values include relatively small but significant contributions from the plasmasphere out to the orbits of the GPS satellites where B_{\parallel} is quite small. Thus, these STEC values are likely somewhat larger than is appropriate for the calculation of ΔB_{\parallel} according to Equation 4, and the resulting ΔB_{\parallel} values may consequently be underestimated to a small degree.

The process by which these calculations are done is illustrated with examples shown in Figures 2 and 3 from 5 August 2019 toward 3C147 and 3C196. In each figure, the top panel shows the unwrapped ϕ_{RR} time series converted to Δ TEC with the instrumental/source bias remaining. The middle panel shows the time series for $\phi_{RR} - \phi_{LL}$ converted to Δ RM in black while the red curve is the Δ TEC values from the top panel multiplied by $B_{\parallel} = b_{\parallel}B$. One can see that these curves are quite similar except for the remaining instrumental/source effects. To calculate ΔB_{\parallel} , the difference was taken between the two curves shown in the middle panel, and the mean difference over the entire 2 hours was subtracted to remove the constant contribution from ϕ_{inst} . These were then divided by the time series for STEC calculated from the JPL IONEX file to arrive at ΔB_{\parallel} , which is shown in the bottom panel. Within these panels, the cyan points show ΔB_{\parallel} averaged within one-minute bins.

We note that if the assumed height for the thin shell approximation is off by an amount Δz , this will add some uncertainty to these calculations. Specifically, the vertical derivative of B_{\parallel} for the observing geometries used here and from the locations of the LWA telescopes is about 10–15 nT km⁻¹. Since Δ TEC is typically within ± 0.1 TECU, this amounts to an uncertainty in Δ TEC B_{\parallel} on the order of Δz TECU nT. As Figures 2 and 3 show, this amounts to a relative error of <2%. Since the typical STEC for our observations is around 10 TECU, the impact on the final value of ΔB_{\parallel} is an uncertainty of $\sim 0.1\Delta z$ nT. This means that a fluctuation in Δ TEC can mimic a ΔB_{\parallel} perturbation if the assumed altitude is incorrect, but that the amplitude will be on the order of a few nT at most (i.e., for an error of a few tens of km). As the results in Sections 2.2 and 2.3 will show, we typically observe fluctuation amplitudes in ΔB_{\parallel} well in excess of this.

In performing this processing on several datasets, it was found that to obtain good results with 3C405 and 3C196, the visibilities needed to be smoothed to 10-s resolution prior to processing. No such smoothing was required for 3C147. The low S/N of 3C461 within the middle of each observing session often made this analysis difficult, especially concerning the unwrapping of phases, and so we have excluded it from the remaining analysis to be presented here. In addition, the S/N and ionospheric impact were both significantly lower within the band centered at 45 MHz. Since good results were routinely obtained at 35 MHz, data from the 45 MHz band were generally superfluous, and analysis of those data are not presented here either.

While 3C147 is the (apparently) brightest source that we used, observing sessions of it and 3C196 were often plagued by radio frequency interference (RFI), and so many more sessions were used to observe 3C405 (and 3C461). Plots of all extracted data for 3C405 are shown in Figure 4. These show the product of ΔB_{\parallel} and STEC as

HELMBOLDT ET AL. 4 of 13

194799x, 2022, 4, Downloaded from https://agupubs.onlinelibrary.wiley.com/doi/10.1029/2021RS007372 by University Of New Mexico, Wiley Online Library on [25/10/2023]. See the Terms and Conditions (https://onlinelibrary.wiley.com/

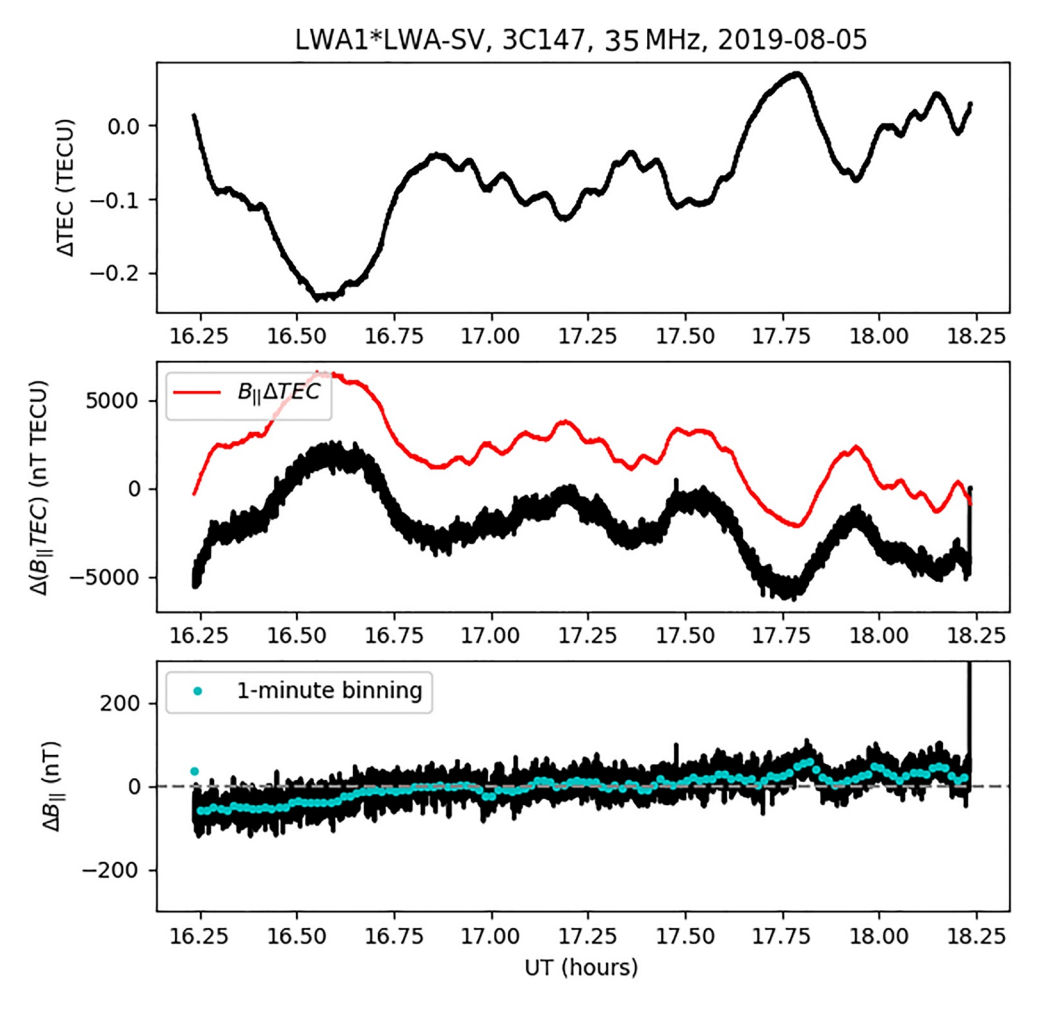


Figure 2. An example of the process of determining ΔB_{\parallel} from an observation of 3C147. Upper: The differential total electron content (TEC; including biases) converted from the RR phase. Middle: The differential rotation measure (black curve) converted from the difference in RR and LL phases with the differential TEC from the upper panel multiplied by the background B_{\parallel} (red curve). Bottom: The differential B_{\parallel} after differencing the two curves in the middle panel (and subtracting the mean) and dividing by the estimated slant TEC from the Jet Propulsion Laboratory IONEX file. Values averaged to one-minute resolution are plotted in cyan.

a function of LST so that we can examine any trends that remain due to the impact of ϕ_{source} (i.e., prior to dividing by STEC, which varies from session to session) and/or the difference in B_{\parallel} between the two telescopes, which is ~100 nT and also repeats in LST. One can see that there is indeed such a trend, but with considerable and significant scatter. We removed this trend by fitting and subtracting a third-order polynomial to/from all of the observations, weighted by σ^{-2} , where σ is the uncertainty per measurement. We repeated this with 3C147 and 3C196 with the results shown in Figures 5 and 6. One can see that the superior S/N achieved with 3C147 makes the deviations from the general LST trend much more obvious. The lack of an obvious trend with LST for this source may also be an indication of its compactness, that is, for a point source, $\phi_{source} = 0$. However, for consistency, we have still subtracted this polynomial fit from the 3C147 data. After subtracting the polynomial fits from the data for all three sources, the results we divided by the JPL IONEX-based STEC time series to generate bias-corrected measurements of ΔB_{\parallel} that will be the subject of the following subsections.

2.2. Magnetic Field Rates

As Figures 4–6 show, beyond the trends with LST caused by instrumental/source effects, there are often temporal gradients that persist throughout the two-hour observations and that change with time of day/year. The rates for ΔB_{\parallel} for each observation were determined with a linear fit after subtracting polynomial fits to the trends with

HELMBOLDT ET AL. 5 of 13

nelibrary.wiley.com/doi/10.1029/2021RS007372 by University Of New Mexico, Wiley Online Library on [25/10/2023]. See the Terms

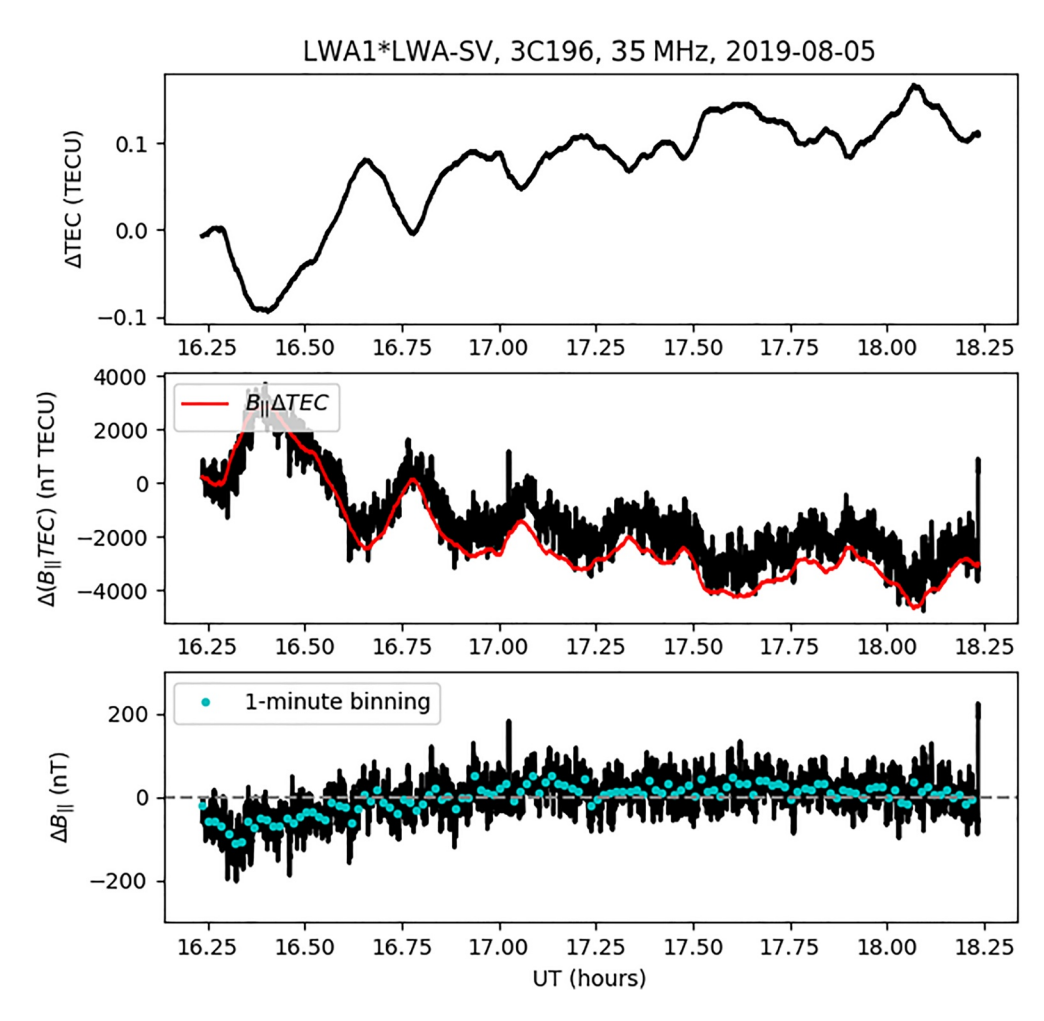


Figure 3. The same as Figure 2, but for 3C196.

LST (see Figures 4–6) and are plotted versus universal time in the upper panel of Figure 7. Despite a noticeable amount of scatter, there is a clear diurnal trend with negative rates apparent before ~15 UT (~8 local time) and positive rates thereafter.

We have compared these with the expected rate of change of B_{\parallel} within each two-hour observation due to the (mostly) vertical gradient in the background electric field. If we assume a purely east/west electric field like the empirical model of Scherliess and Fejer (1999) and that the field lines are equi-potentials, then

$$\vec{E} = \frac{R_0 \cos \lambda_0}{R \cos \lambda} E_0 \hat{i} \tag{5}$$

where the naught subscript denotes values at a reference altitude (nominally 300 km) and \hat{i} points toward east. Here, λ is geomagnetic latitude and R is the distance from the center of the Earth. If we assume that the north/south coordinate $y \approx R(\lambda - \lambda_0)$ and the vertical coordinate $z \approx R - R_e$ (R_e is the radius of the Earth), then from Faraday's law of induction

$$\dot{\vec{B}}_0 \approx \frac{E_0}{R_0} \hat{j} + \frac{E_0}{R_0} \tan \lambda_0 \hat{k} \tag{6}$$

where \hat{j} and \hat{k} point northward and vertically, respectively. It then follows that for the thin shell approximation, $\dot{B}_{\parallel} \approx \hat{s} \cdot \dot{B}_{0}$, where the unit vector \hat{s} points along the line of sight. For all sources and observing session, the north/south component of \hat{s} was between 0.05 and 0.25 and the vertical component ranged from 0.87 to 0.98. Thus, the \hat{k} component of \dot{B}_{0} tended to dominate \dot{B}_{\parallel} .

HELMBOLDT ET AL. 6 of 13

. 2022, 4, Downloaded from https://agupubs.onlinelibrary.wiley.com/doi/10.1029/2021RS007372 by University Of New Mexico, Wiley Online Library on [25/10/2023]. See the Terms

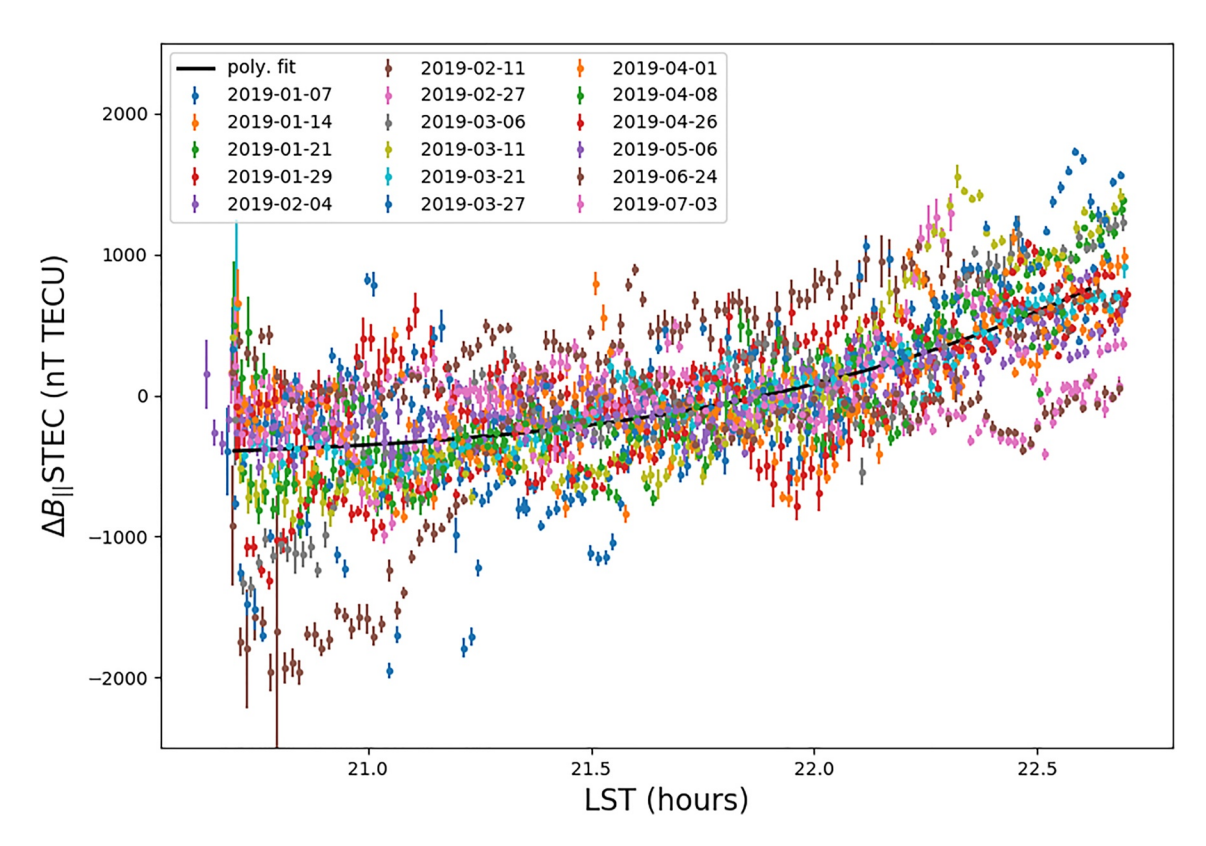


Figure 4. For all observations of 3C405, the product of ΔB_{\parallel} and slant TEC versus local sidereal time . The black curve is a third-order polynomial fit used to remove any remaining instrumental and/or source biases.

To calculate \dot{B}_{\parallel} for our observations, we used the vertical drift model of Scherliess and Fejer (1999) with an assumed ionospheric magnetic field magnitude of 4×10^{-5} T to compute E_0 . We also assumed a reference altitude of 300 km and $\lambda_0 = 41.8^{\circ}$ (the geomagnetic latitude of LWA1). The curves in the upper panel of Figure 7 show the computed values of \dot{B}_{\parallel} , and they follow the ordinate on the right. These curves follow a similar pattern as the measured ΔB_{\parallel} rates, albeit with an offset. Specifically, if the model values are assumed to be the true \dot{B}_{\parallel} at LWA1, then the data are consistent with $\dot{B}_{\parallel,SV} \approx 0.75\,\dot{B}_{\parallel,1} + 50$ nT hr⁻¹. This trend implies that the electric fields at the two LWA stations generally follow a similar but slightly different diurnal pattern with ΔE_0 ranging from -0.2 to 0.1 mV m⁻¹ during the dates/times covered by our observing sessions. For comparison, the Scherliess and Fejer (1999) model predicts that E_0 ranges from -0.5 to 0.8 mV m⁻¹ during the same dates/times. We note that these quantities are rough estimates since they all depend on the assumption that the east/west electric field specified by the Scherliess and Fejer (1999) model is valid/appropriate.

2.3. Magnetic Field Oscillations

To quantify fluctuations in the magnetic field on time scales shorter than $\sim 1-2$ hr, each time series of ΔB_{\parallel} was de-trended by subtracting a linear fit. The power spectra for the de-trended time series for 3C405 are displayed in Figure 8 with the left and right ordinates showing the UT and day of the year for each spectrum, respectively. Since the sources were always observed near transit, there is a linear relationship between day of the year and the time 3C405 was observed. One can see that fluctuations with oscillation periods of $\sim 0.5-1$ hr were fairly common, but periods as short as 6 min (frequency of 10 hr^{-1}) were observed between 15 and 17 UT in the spring ($\sim 8-10$ local time).

These oscillation periods are broadly consistent with gravity wave-driven TIDs. To further test this notion, the speeds of such disturbances were constrained by examining the time series that were measured simultaneously for 3C147 and 3C196. These are shown before de-trending in the panels of Figure 9. One can see that the observed gradients generally agree between the two sources. There are also several instances of obvious oscillations within

HELMBOLDT ET AL. 7 of 13

1944/799x, 2022, 4, Downloaded from https://agupubs.onlinelibrary.wiley.com/doi/10.1029/2021RS007372 by University Of New Mexico, Wiley Online Library on [25/10/2023]. See the Terms and Conditions (https://onlinelibrary.wiley.com/erms-and-conditions) on Wiley Online Library for rules of use; OA articles are governed by the applicable Crea

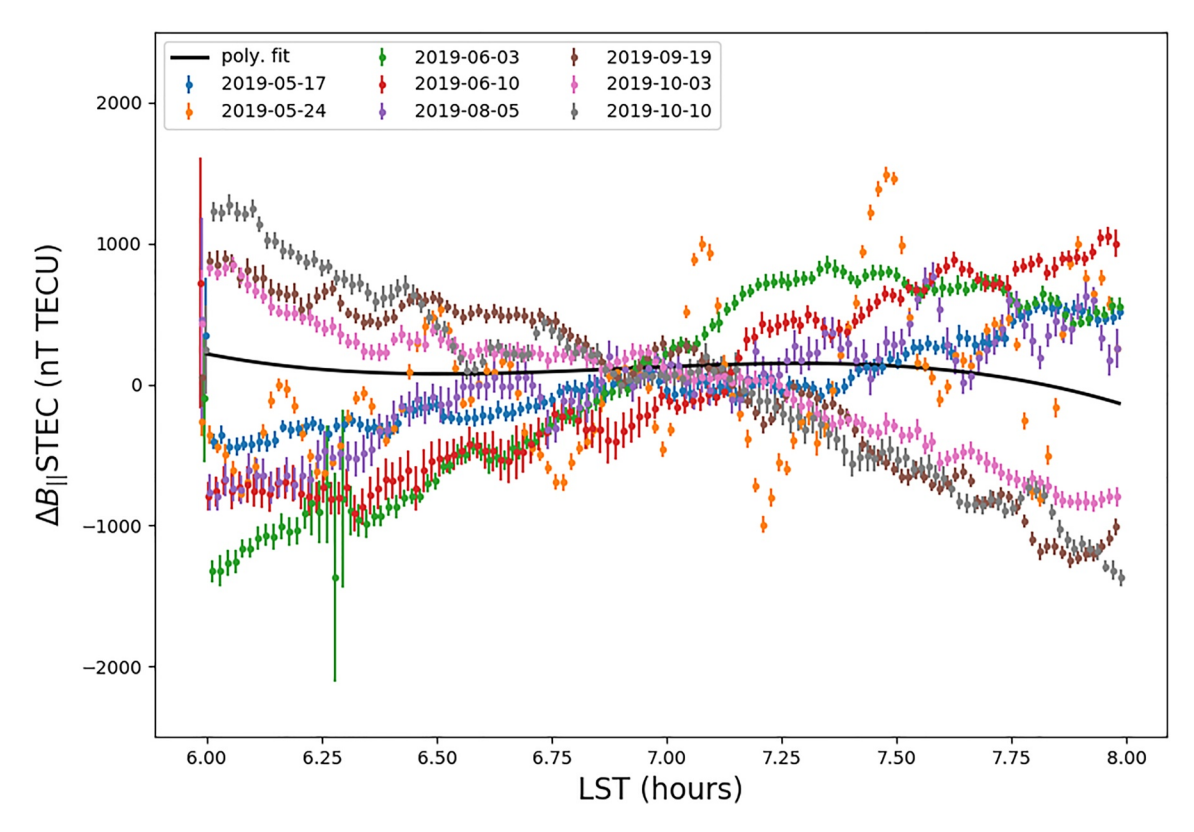


Figure 5. The same as Figure 4, but for 3C147.

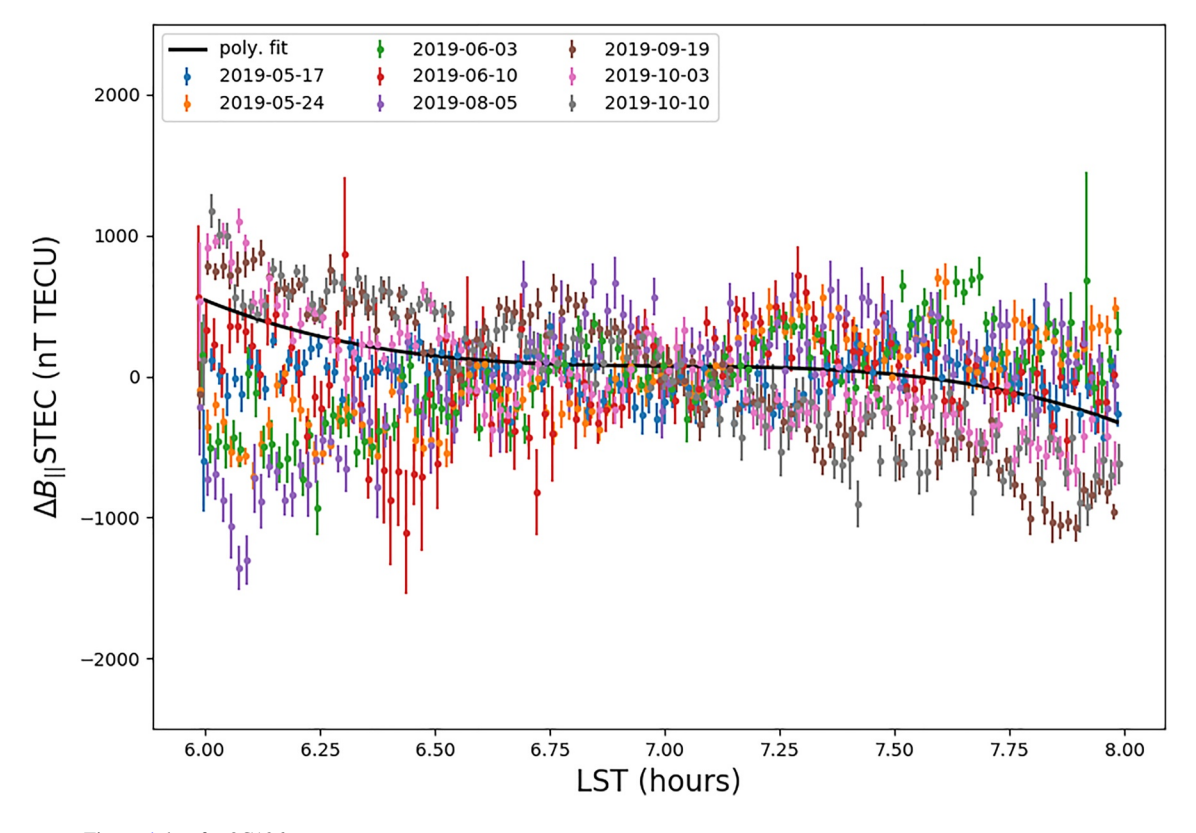


Figure 6. The same as Figure 4, but for 3C196.

HELMBOLDT ET AL. 8 of 13

1944799x, 2022, 4, Downloaded from https://agupubs.onlinelibrary.wiley.com/doi/10.1029/2021RS007372 by University Of New Mexico, Wiley Online Library on [25/10/2023]. See the Terms

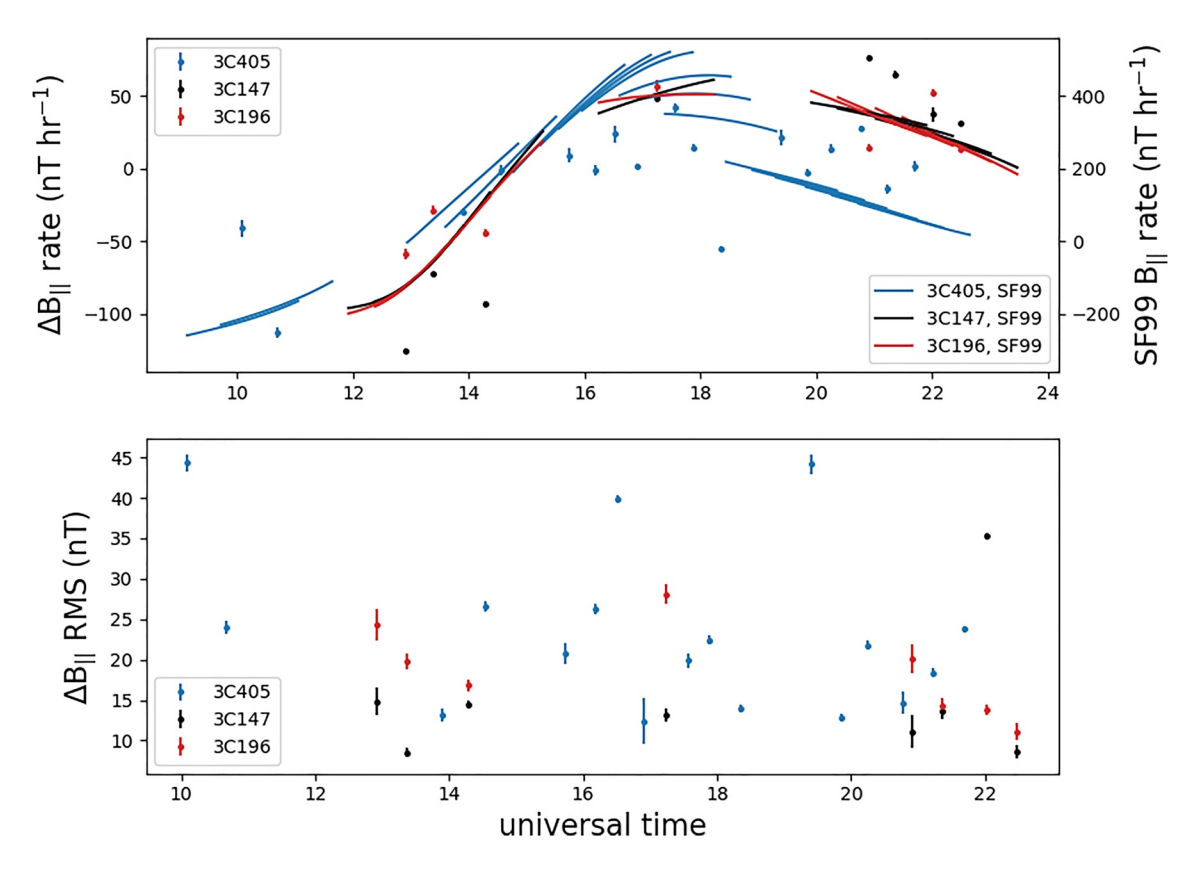


Figure 7. Upper: The ΔB_{\parallel} rate computed per observing session and per source as a function of universal time as points (left ordinate) and estimates for \dot{B}_{\parallel} due to the vertical gradient in the electric field given by Scherliess and Fejer (1999) (SF99 in the legend) as curves (right ordinate). Lower: The RMS variation in ΔB_{\parallel} per observing session and per source.

one or both time series. To focus on the possibility that the lines of sight toward these two sources were probing different parts of the same TID, we de-trended the time series and computed the cross correlation function between the two for each observing session. These are plotted in the right column of panels in Figure 10 with fluctuation power spectra for both sources plotted in the corresponding panels to the left. For a plane wave, the cross correlation function will have positive peaks at lags of $\Delta x/v_x + nP$ and negative peaks at $\Delta x/v_x + (n + 0.5)$ P, where v_x is the wave's phase velocity projected along the vector separating the two sources, P is the period, and n is an integer. 3C147 and 3C196 are separated on the sky by 25.4°. During our observations (i.e., near transit for each), the separation was mostly in the east/west direction with $\Delta x \approx 140$ km at an altitude of 300 km.

Deviations from a simple plane wave will alter the appearance of the cross correlation function for an actual TID. Still, most of the panels in the right column of Figure 10 exhibit behavior similar to the expected pattern. The locations of the positive and negative peaks imply $v_x \approx 90$ –230 m s⁻¹ (lags ~10–25 min) and periods from ~10 min to nearly an hour, which are consistent with the spectra shown in the left column of Figure 10. To assess the significance of the peaks within each cross correlation function, the calculation was repeated 100 times with the time series for 3C196 resorted according to a series of randomly generated numbers. The upper and lower boundaries of the purple shaded region within each panel show the 10^{th} and 90^{th} percentiles from the randomized recalculations with the curve in the middle representing the median. Nearly all the peaks evident within the cross correlation functions are above/below the $90^{th}/10^{th}$ percentile, strongly indicating that they are not the result of random chance correlations.

The results above imply a typical wavelength of roughly 300 km and a ΔB_{\parallel} amplitude of about 15 nT. Since the LWA stations are separated by 75 km, this implies a B_{\parallel} amplitude of about 20 nT. Furthermore, if we assume an oscillation period of 30 min (frequency = 2 hr⁻¹), the amplitude of the fluctuation in \dot{B}_{\parallel} would be approximately 250 nT hr⁻¹. From Equation 6, this requires a fluctuation in the background electric field of roughly 0.5 mV m⁻¹ at 300 km altitude. A gravity wave with a vertically-integrated wind amplitude on the order of 10 m s⁻¹

HELMBOLDT ET AL. 9 of 13

1944799x, 2022, 4, Downloaded from https://agupubs.onlinelibrary.wiley.com/doi/10.1029/2021RS007372 by University Of New Mexico, Wiley Online Library on [25/10/2023]. See the

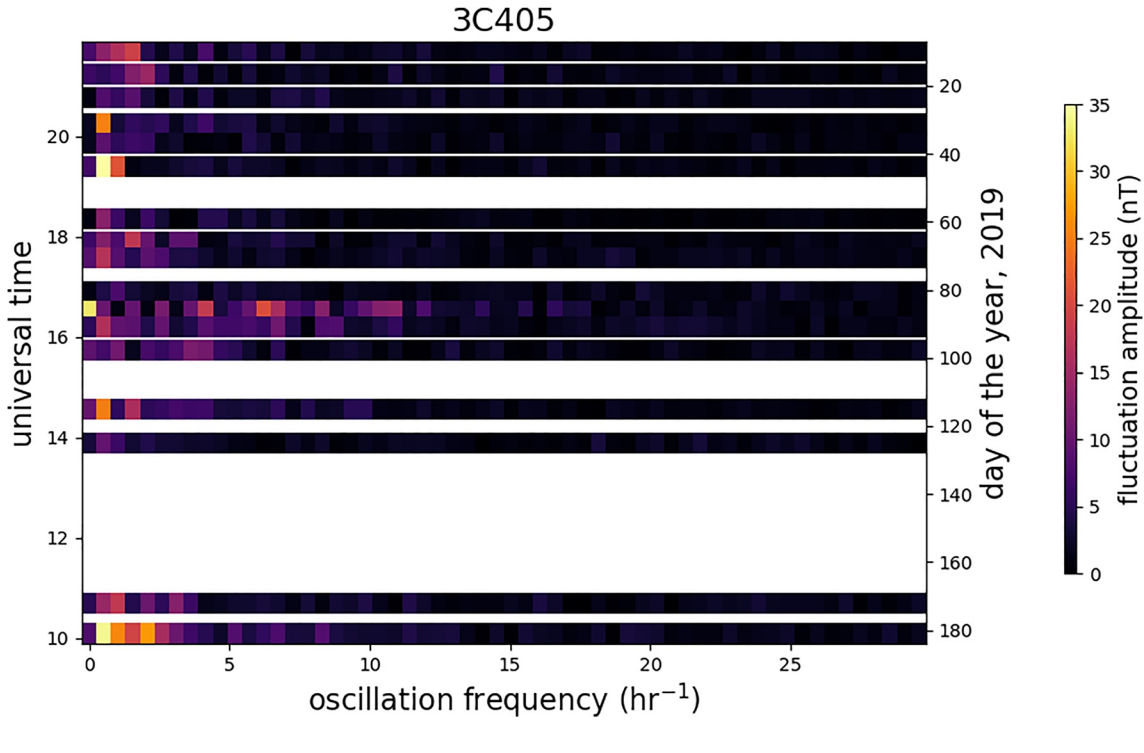


Figure 8. Fluctuation amplitude as a function of universal time/day of the year and oscillation frequency for ΔB_{\parallel} measurements made with 3C405.

within the dynamo region (~110–170 km altitude) could cause this. This is well within the expected range of amplitudes for gravity waves of this size in the upper mesosphere/lower thermosphere region (e.g., Becker and Vadas, 2018, 2020). In addition, an electric field fluctuation amplitude of 0.5 mV m⁻¹ is consistent with the properties of nighttime, medium scale TIDs, which are often referred to as electro-buoyancy waves due to the polarization electric fields that form along their wavefronts (e.g., Shiokawa et al., 2003; Helmboldt et al., 2020).

3. Conclusions

The results presented here demonstrate a novel method for characterizing fluctuations in the magnetic field within the mid-latitude ionosphere. They generally demonstrate that on a scale of 75 km, while there is a measurable amount of differential Faraday rotation, the impact is likely minimal for microwave and meter-wave frequencies. The plots in Figures 2 and 3 show that the amplitude of Δ RM was at most 5,000 TECU nT, or 0.01 radians m⁻². This is comparable to broadband (22–70 MHz) Low Frequency Array (LOFAR) observations of Δ RM reported by de Gasperin et al. (2018). From Equation 2, this implies a difference in RR and LL phases of 1.5° and 0.06° at wavelengths of 1-m and 20-cm, respectively. Thus, the error caused by the differential Faraday rotation within the measured electric vector position angle at these frequencies is relatively small but still significant. At 35 MHz, the corresponding error is 110°. This is much more significant, but is not as relevant given the general lack of cosmic radio sources that exhibit polarized emission at this frequency. Notable exceptions to this are bursts of emission from the Sun (Melrose, 1980) and Jupiter (Clarke et al., 2014) as well as flares from active stars (Callingham et al., 2021; Davis et al., 2020). Any effort to image these phenomena with high resolution at a comparable frequency must therefore account for this effect, for example, with LOFAR (Breitling et al., 2015).

In addition, for a linearly polarized source, the measured polarized intensity will be degraded by a factor of $\exp\left[-\left\langle \left(\phi_{RR}-\phi_{LL}\right)^{2}\right\rangle\right]$. For the numbers quoted above at 1-m and 20-cm wavelength, this factor is nearly indistinguishable from unity. At 35 MHz however, this drops to 0.03 and thus cannot be ignored at relatively low frequencies. We also note that Δ RM appears to be driven mostly by differences in TEC rather than perturbations within the magnetic field. The outer scale beyond which the phase/TEC structure function flattens is typically ~30 km (Nickisch et al., 2012), and so Δ RM is not likely to be appreciably larger on baselines longer than the 75-km one used here. Therefore, the results imply that degradation of polarized intensity by differential Faraday

HELMBOLDT ET AL. 10 of 13

1944799x, 2022, 4, Downloaded from https://agupubs.onlinelibrary.wiley.com/doi/10.1029/2021RS007372 by University Of New Mexico, Wiley Online Library on [25/10/2023]. See the Terms

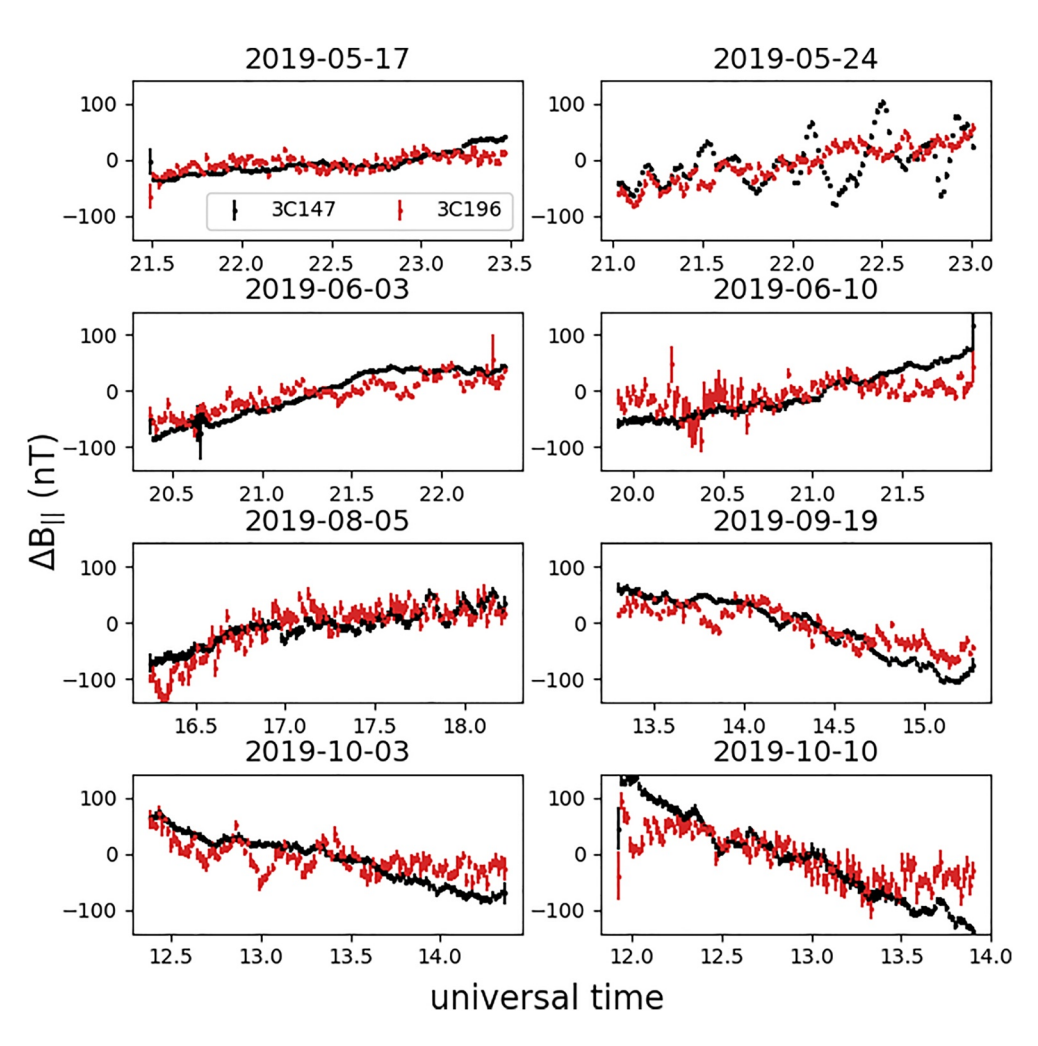


Figure 9. ΔB_{\parallel} time series from concurrent observations of 3C147 (black) and 3C196 (red).

rotation will generally not be an issue for the next generation of microwave/meter-wave instruments such as the SKA and ngVLA. However, on comparably long baselines, it will have a noticeable impact on the accuracy of polarization angle measurements, especially within the lowest frequency bands. Furthermore, the results from 3C196 to 3C147 have implications for wide-field polarimetry as the RM for these two sources separated by $\sim 25^{\circ}$ degrees can differ by as much as a few thousand TECU nT, or on the order of 0.005–0.01 radians m⁻².

Apart from practical considerations for radio astronomy, the results of this study offer unique insights into the dynamics of Earth's magnetic field within the mid-latitude ionosphere. Differences in B_{\parallel} on time scales comparable to the observing sessions (\sim 2 hr) appear to be largely driven by small differences in the electric field between the two stations' lines of sight. These manifest as ΔB_{\parallel} rates with magnitudes as large as 100 nT hr⁻¹. On smaller temporal scales, the RMS variations in ΔB_{\parallel} were typically \sim 10–30 nT with wavelike fluctuations often apparent. The oscillation periods of these appear broadly consistent with gravity waves/TIDs, and the wind amplitudes required to reproduce the observed properties are \sim 10 m s⁻¹, which is reasonable for gravity waves within the upper atmosphere. These are also consistent with electric field disturbances with amplitudes on the order of 0.5 mV m⁻¹, which is comparable to the typical magnitude of the background electric field.

We have demonstrated that a low-frequency (35 MHz) interferometer can be a useful and novel tool for measuring subtle changes within Earth's magnetic field at ionospheric heights, even when observing unpolarized cosmic radio sources. While these magnetic field perturbations do not appear to be an issue for high angular resolution astronomical polarimetry, they do illustrate the need to account for localized variations in the ionospheric electric field, which are not reproduced by empirical/climatological models. The observations indicate that while the diurnal variation in the electric field is consistent with such models, it can differ significantly (as much as

HELMBOLDT ET AL. 11 of 13

1944/799x, 2022, 4, Downloaded from https://agupubs.onlinelibrary.wiley.com/doi/10.1029/2021R8007372 by University Of New Mexico, Wiley Online Library on [25/10/2023]. See the Terms and Conditions (https://onlinelibrary.wiley

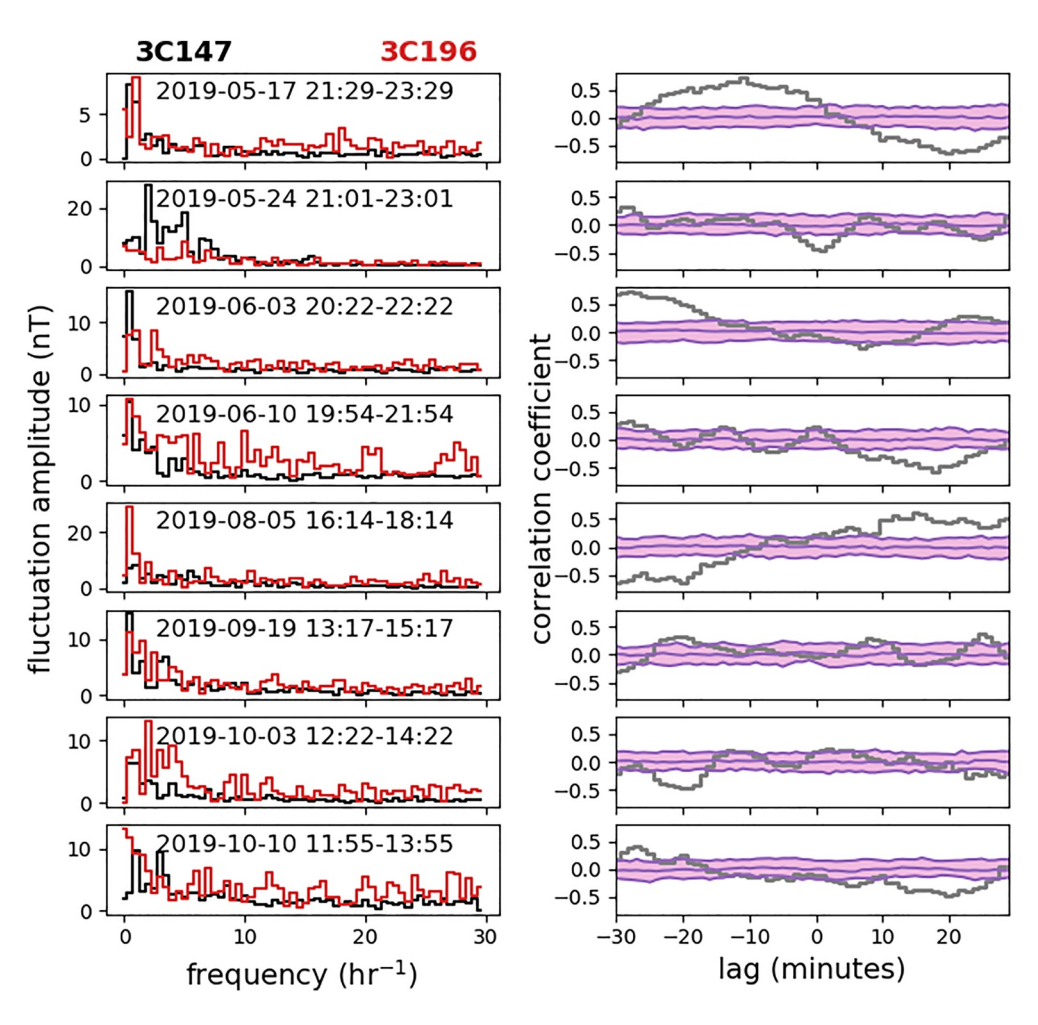


Figure 10. Left column: ΔB_{\parallel} fluctuation spectra from concurrent observations of 3C147 (black) and 3C196 (red). Right column: Cross correlation functions for the ΔB_{\parallel} time series from 3C147 to 3C196 corresponding to the spectra shown to the left. The purple-shaded regions span the 10th and 90th percentiles from 100 randomized recalculations of the cross correlation function with the curve in the middle indicating the median.

 \sim 10%–20%) between two locations separated by just 75 km. In addition, observed magnetic field oscillations are consistent with gravity wave-driven electric field perturbations with amplitudes that rival the background electric field. This demonstrates how a three-dimensional potential solver coupled to accurate specifications of local thermospheric conditions (e.g., Huba et al., 2008) is required to properly capture the nature of the ionospheric electric field.

Data Availability Statement

The LWA data used within this publication are available from the LWA data archive under project LH015 (https://lda10g.alliance.unm.edu/ldadb/project_detail/263/). JPL IONEX files are available at https://cddis.nasa.gov/archive/gnss/products/ionex; access requires registration with and/or logging into NASA's EARTHDATA system (https://earthdata.nasa.gov).

References

Becker, E., & Vadas, S. L. (2018). Secondary gravity waves in the winter mesosphere: Results from a high-resolution global circulation model. Journal of Geophysical Research: Atmospheres, 123(5), 2605–2627. https://doi.org/10.1002/2017JD027460

Becker, E., & Vadas, S. L. (2020). Explicit global simulation of gravity waves in the thermosphere. Journal of Geophysical Research: Space

Acknowledgments

Basic research at the Naval Research Laboratory (NRL) is supported by 6.1 base funding. Construction of the LWA has been supported by the Office of Naval Research under Contract N00014-07-C-0147 and by the AFOSR. Support for operations and continuing development of the LWA1 is provided by the Air Force Research Laboratory and the National Science Foundation under grants AST-1835400 and AGS-1708855.

HELMBOLDT ET AL. 12 of 13

Physics, 125(10), e2020JA028034. https://doi.org/10.1029/2020JA028034

1944799x,

are governed by the applicable Crea

- Breitling, F., Mann, G., Vocks, C., Steinmetz, M., & Strassmeier, K. G. (2015). The LOFAR solar imaging pipeline and the LOFAR solar data center. *Astronomy and Computing*, 13, 99–107. https://doi.org/10.1016/j.ascom.2015.08.001
- Callingham, J. R., Pope, B. J. S., Feinstein, A. D., Vedantham, H. K., Shimwell, T. W., Zarka, P., et al. (2021). Low-frequency monitoring of flare star binary CR draconis: Long-term electron-cyclotron maser emission. *Astronomy and Astrophysics*, 648, A13. https://doi.org/10.1051/0004-6361/202039144
- Clarke, T. E., Higgins, C. A., Skarda, J., Imai, K., Imai, M., Reyes, F., et al. (2014). Probing jovian decametric emission with the long wavelength array station 1. *Journal of Geophysical Research: Space Physics*, 119(12), 9508–9526. https://doi.org/10.1002/2014JA020289
- Davis, I., Taylor, G., & Dowell, J. (2020). Observing flare stars below 100 mhz with the lwa. Monthly Notices of the Royal Astronomical Society, 494(4), 4848–4853. https://doi.org/10.1093/mnras/staa988
- de Gasperin, F., Mevius, M., Rafferty, D. A., Intema, H. T., & Fallows, R. A. (2018). The effect of the ionosphere on ultra-low-frequency radio-interferometric observations. *Astronomy and Astrophysics*, 615, A179. https://doi.org/10.1051/0004-6361/201833012
- de Gasperin, F., Vink, J., McKean, J. P., Asgekar, A., Avruch, I., Bentum, M. J., et al. (2020). Cassiopeia A, Cygnus A, Taurus A, and Virgo A at ultra-low radio frequencies. Astronomy and Astrophysics. 635, A150. https://doi.org/10.1051/0004-6361/201936844
- Helmboldt, J. F., Haiducek, J. D., & Clarke, T. E. (2020). The properties and origins of corotating plasmaspheric irregularities as revealed through a new tomographic technique. *Journal of Geophysical Research: Space Physics*, 125(3), e2019JA027483. https://doi.org/10.1029/2019JA027483
- Hickey, M. P., Schubert, G., & Walterscheid, R. L. (2009). Propagation of tsunami-driven gravity waves into the thermosphere and ionosphere. Journal of Geophysical Research, 114(A8), 8304. https://doi.org/10.1029/2009JA014105
- Hooke, W. H. (1968). Ionospheric irregularities produced by internal atmospheric gravity waves. *Journal of Atmospheric and Terrestrial Physics*, 30(5), 795–823. https://doi.org/10.1016/S0021-9169(68)80033-9
- Huba, J. D., Drob, D. P., Wu, T. W., & Makela, J. J. (2015). Modeling the ionospheric impact of tsunami-driven gravity waves with Sami3: Conjugate effects. *Geophysical Research Letters*, 42(14), 5719–5726. https://doi.org/10.1002/2015GL064871
- Huba, J. D., Joyce, G., & Krall, J. (2008). Three-dimensional equatorial spread F modeling. Geophysical Research Letters, 35(10), L10102. https://doi.org/10.1029/2008GL033509
- Lühr, H., & Maus, S. (2006). Direct observation of the F region dynamo currents and the spatial structure of the EEJ by CHAMP. Geophysical Research Letters. 33(24), L24102. https://doi.org/10.1029/2006GL028374
- Maus, S., & Lühr, H. (2006). A gravity-driven electric current in the Earth's ionosphere identified in CHAMP satellite magnetic measurements.
- Geophysical Research Letters, 33(2), L02812. https://doi.org/10.1029/2005GL024436

 Melrose, D. B. (1980). The emission mechanisms for solar radio bursts. Space Science Reviews, 26(1), 3–38. https://doi.org/10.1007/BF00212597
- Murphy, E. J., Bolatto, A., Chatterjee, S., Casey, C. M., Chomiuk, L., Dale, D., et al. (2018). The ngVLA science case and associated science requirements. In E.Murphy (Ed.), Science with a next generation very large array (Vol. 517, pp. 3).
- Nickisch, L. J., St John, G., Fridman, S. V., Hausman, M. A., & Coleman, C. J. (2012). Hicirf: A high-fidelity hf channel simulation. *Radio Science*, 47(4), RS0L11. https://doi.org/10.1029/2011RS004928
- Otsuka, Y., Shiokawa, K., Ogawa, T., & Wilkinson, P. (2004). Geomagnetic conjugate observations of medium-scale traveling ionospheric disturbances at midlatitude using all-sky airglow imagers. *Geophysical Research Letters*, 31(15), L15803. https://doi.org/10.1029/2004GL020262
- Park, J., Lühr, H., Stolle, C., Rother, M., Min, K. W., & Michaelis, I. (2009). The characteristics of field-aligned currents associated with equatorial plasma bubbles as observed by the CHAMP satellite. *Annales Geophysicae*, 27(7), 2685–2697. https://doi.org/10.5194/angeo-27-2685-2009
- Perkins, F. (1973). Spread F and ionospheric currents. *Journal of Geophysical Research*, 78(1), 218–226. https://doi.org/10.1029/JA078i001p00218

 Quinn, P., Axelrod, T., Bird, I., Dodson, R., Szalay, A., & Wicenec, A. (2015). Delivering SKA science. In *Advancing astrophysics with the square kilometre array* (aaskal4) (p. 147).
- Scherliess, L., & Fejer, B. G. (1999). Radar and satellite global equatorial f region vertical drift model. *Journal of Geophysical Research*, 104(A4), 6829–6842. https://doi.org/10.1029/1999JA900025
- Shiokawa, K., Otsuka, Y., Ihara, C., Ogawa, T., & Rich, F. J. (2003). Ground and satellite observations of nighttime medium-scale traveling ionospheric disturbance at midlatitude. *Journal of Geophysical Research*, 108(A4), 1145. https://doi.org/10.1029/2002JA009639
- Taylor, G. B., Ellingson, S. W., Kassim, N. E., Craig, J., Dowell, J., Wolfe, C. N., et al. (2012). First light for the first station of the long wavelength array. *Journal of Astronomical Instrumentation*, 1(01), 50004. https://doi.org/10.1142/S2251171712500043
- Tsuda, T. (2014). Characteristics of atmospheric gravity waves observed using the MU (middle and upper atmosphere) radar and GPS (global positioning system) radio occultation. *Proceeding of the Japan Academy, Series B*, 90(1), 12–27. https://doi.org/10.2183/pjab.90.12
- Vadas, S. L., & Crowley, G. (2010). Sources of the traveling ionospheric disturbances observed by the ionospheric TIDDBIT sounder near Wallops Island on 30 October 2007. *Journal of Geophysical Research*, 115(A7), 7324. https://doi.org/10.1029/2009JA015053
- Vadas, S. L., & Fritts, D. C. (2002). The importance of spatial variability in the generation of secondary gravity waves from local body forces. Geophysical Research Letters. 29(20), 1984, https://doi.org/10.1029/2002GL015574
- Yamazaki, Y., & Maute, A. (2017). Sq and EEJ—a review on the daily variation of the geomagnetic field caused by ionospheric dynamo currents. Space Science Reviews, 206(1-4), 299-405. https://doi.org/10.1007/s11214-016-0282-z

HELMBOLDT ET AL. 13 of 13